

## RESEARCH ARTICLE

# Patch formation driven by stochastic effects of interaction between viruses and defective interfering particles

Qiantong Liang  <sup>1</sup>, Johnny Yang <sup>2</sup>, Wai-Tong Louis Fan <sup>2,3</sup>, Wing-Cheong Lo  <sup>1\*</sup>

**1** Department of Mathematics, City University of Hong Kong, Hong Kong, China, **2** Department of Mathematics, Indiana University, Bloomington, Indiana, United States of America, **3** Department of Organismic and Evolutionary Biology, Harvard University, Cambridge, Massachusetts, United States of America

\* [wingclo@cityu.edu.hk](mailto:wingclo@cityu.edu.hk)



## OPEN ACCESS

**Citation:** Liang Q, Yang J, Fan W-TL, Lo W-C (2023) Patch formation driven by stochastic effects of interaction between viruses and defective interfering particles. PLoS Comput Biol 19(10): e1011513. <https://doi.org/10.1371/journal.pcbi.1011513>

**Editor:** James M McCaw, The University of Melbourne, AUSTRALIA

**Received:** February 7, 2023

**Accepted:** September 12, 2023

**Published:** October 2, 2023

**Copyright:** © 2023 Liang et al. This is an open access article distributed under the terms of the [Creative Commons Attribution License](#), which permits unrestricted use, distribution, and reproduction in any medium, provided the original author and source are credited.

**Data Availability Statement:** All relevant data are within the manuscript and its [Supporting information](#) files.

**Funding:** QL was partially supported by University Grants Committee (UGC) in Hong Kong. WCL was supported by RGC General Research Fund (Project No. CityU 11301821). WTLF and JY were supported by National Science Foundation grants (DMS-1855417 571 and DMS-2152103), and Office of Naval Research grant (N00014-20-1-2411). The funders had no role in study design,

## Abstract

Defective interfering particles (DIPs) are virus-like particles that occur naturally during virus infections. These particles are defective, lacking essential genetic materials for replication, but they can interact with the wild-type virus and potentially be used as therapeutic agents. However, the effect of DIPs on infection spread is still unclear due to complicated stochastic effects and nonlinear spatial dynamics. In this work, we develop a model with a new hybrid method to study the spatial-temporal dynamics of viruses and DIPs co-infections within hosts. We present two different scenarios of virus production and compare the results from deterministic and stochastic models to demonstrate how the stochastic effect is involved in the spatial dynamics of virus transmission. We compare the spread features of the virus in simulations and experiments, including the formation and the speed of virus spread and the emergence of stochastic patchy patterns of virus distribution. Our simulations simultaneously capture observed spatial spread features in the experimental data, including the spread rate of the virus and its patchiness. The results demonstrate that DIPs can slow down the growth of virus particles and make the spread of the virus more patchy.

## Author summary

Defective interfering particles (DIPs) are viral mutants in which a crucial part of the particle's genome has been lost. DIPs are not infectious but can still co-infect cells with natural viruses. Such mutations are not uncommon. In fact, it has been found in most classes of viruses, including SARS coronavirus and influenza virus. It gives DIPs a promising future as a medium for disease treatment. However, the mechanism by which DIPs affect virus transmission remains unclear. In this paper, we develop a model to study the interaction between viruses and DIPs within host cells and the role stochastic effects play in virus transmission. Our simulations can capture patchy patterns and other spatial spread

data collection and analysis, decision to publish, or preparation of the manuscript.

**Competing interests:** The authors have declared that no competing interests exist.

features observed in experiments and demonstrate that DIPs can slow down the growth of virus particles and make the spread of viruses more patchy.

## Introduction

Many diseases such as COVID-19, Ebola virus disease, AIDS, and SARS, are caused by the transmission of viruses. Various antiviral drugs have been proposed to inhibit the gene and protein functions of viruses. Still, a major challenge in drug development is caused by occasional mutations in the viral genomes. However, some of these mutations may help us create a new type of treatment through developing defective interfering particles (DIPs), which are virus-like particles that have been detected in patients infected with influenza A virus [1], and with dengue virus, as well as birds infected with West Nile virus [2]. DIPs lack some viral genes that are essential for replication. But, when they co-infect a cell with viable viruses, DIPs divert replication or packaging resources from the virus towards their own growth, thereby compromising normal virus growth [1, 3]. The mechanism of viral material egress is very complex [4], and many factors have been shown to influence it [5, 6], such as empty capsid [7]. In this work, we are focusing specifically on the effect of DIPs on virus production. The competition between infectious viruses and DIPs for the resources in a host may induce a delay and decrease in infectious virus production [3, 8]. For example, in the recent work [9], a combined experimental evolution and computational approach identified defective viral genomes that optimally interfere with Zika virus infection and show antiviral activity in mice and mosquitoes. Therefore, DIPs interfere with virus production, a feature that underscores their promise as therapeutic agents [9–12].

In a recent experimental study [3], engineered reporter viruses and DIP were constructed, which enabled measurement of the gene expressions of both viral and DIP during co-infection of susceptible host cells. Quantitative microscopy imaging in [3] demonstrated that levels of virus and DIP production from co-infected cells can be highly sensitive to their input ratios (multiplicities of infection, MOI), and revealed diverse spatial patterns during co-infection spread. The experimental results showed that viral gene expression was more delayed and that patterns of spread became more “patchy” with a higher level of DIPs to the initial cell. However, it is not clear that how the timing and level of this spatial distribution of DIP expression are related to the spread of virus infection, and what are the key mechanisms responsible for the diverse spatial patterns of the virus and DIP levels.

Many mathematical models were built to study the growth of virus [13–22] and the interaction of DIPs and viruses [23–28]. The simulations and analyses provide us a theoretical idea to understand the development of infectious diseases and how to control the growth of viruses. For example, in [23], a simple mathematical model was proposed for studying the deterministic chaos caused by DIPs. However, there are not many models considering the spatial effect of the interaction of DIPs and viruses in a one- or two-dimensional domain. Frank [24] developed a one-dimensional partial differential equation model for studying the dynamics of the populations of DIPs and viruses within hosts. His work studied how the dynamics of virus spreading depend on the rate at which killed host cells are replaced. These results explain the key processes that control the diversity of observed experimental outcomes and provide a stepping stone to study the spatial model of the transmissions of DIPs and viruses. A two-dimensional domain has to be considered for

reproducing the patchy pattern. Akpinar et al. [25] built a two-dimensional computational model, adapting a cellular automaton approach to incorporate kinetic data on virus growth, but the model is not able to capture the spread rate and the spatial patterns simultaneously observed in [3].

The existing computational studies provide a keystone for modeling the interaction of DIPs and wild-type viruses. However, the mechanism by which DIPs affect the spatial distribution of virus expression is still unclear partly due to complicated stochastic effects and nonlinear spatial dynamics. In [29], the authors applied a stochastic model to study different solutions for continuous and burst production of virions which cannot be studied through deterministic models. In [30], a hybrid stochastic-deterministic computational model was applied to capture experimentally observed variation in the fitness difference between two virus strains. The simulations of the model suggest a way to minimize the variation and dual infection in experiments. In [31], a stochastic model was built to study the effect of DIPs and the results support that DIPs have a slowing effect on the growth of viral plaques, but the spread features are not quantified in that study. These computational studies suggest that stochastic effects play an important role in virus spreading, but the stochastic effects in the virus and DIP transmissions are poorly understood. It inspires us to build a stochastic spatial model to study the interaction of DIPs and viruses and how the effect of DIPs leads to patchy patterns of virus expression observed in experiments.

In this paper, we develop and analyze a new mathematical model to study the spreading speed and the spatial pattern generated by the interaction of viruses and DIPs. To incorporate the random movements of the virus and the DIPs and the stochastic effect of the interactions due to finite number of particles, we developed a stochastic reaction-diffusion system for the virus and DIP co-infection and built a hybrid method for stochastic simulation. Our stochastic model enables also the study and comparison of two common scenarios of virus production. Our simulation results demonstrated that this model can regenerate simultaneously the patchy patterns and the spread rates observed in wet-lab experiments [3], which was not achieved in previous studies [25].

## Modeling

Our new hybrid model is developed based on the deterministic reaction-diffusion model introduced by Frank [24], but has several differences and new features. Importantly, our model and simulation results capture spatial spread features in two-dimensions observed in experiments and overcome computational challenges in stochastic simulations in two-dimensional domains, while the results in [24] are for one-dimension. Furthermore, we introduced and compared two different scenarios of virus production in the stochastic simulations.

Below we describe firstly the deterministic part of our model which is a system of partial differential equations, and secondly our stochastic model that incorporates two different scenarios of virus production.

## Deterministic model

Based on the model in [24], we propose a new model which includes the virus and DIP productions. As shown in Fig 1, in the model, we consider free natural infectious virus, denoted by  $V(t, \vec{x})$ , and defective interfering particles (DIPs), denoted by  $D(t, \vec{x})$  where  $\vec{x} = (x_1, x_2)$  is a vector which represents a spatial location in a two-dimensional domain  $[0, x_{1\max}] \times [0, x_{2\max}]$ . Also, there are six types of cells: uninfected cells, cells infected only by natural viruses but not in the period of virus production, cells infected only by natural viruses and in the period of virus

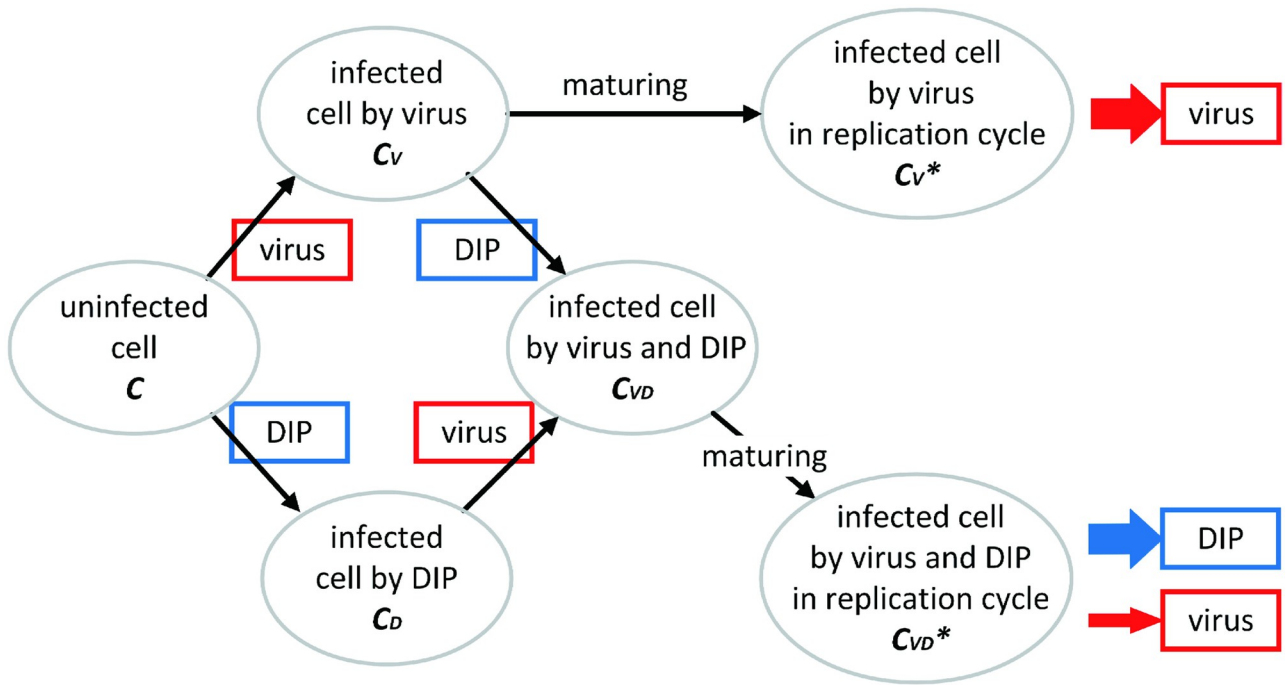


Fig 1. Schematic diagram of the virus-DIPs system.

<https://doi.org/10.1371/journal.pcbi.1011513.g001>

production, cells infected by DIPs only, cells infected by DIPs and natural viruses but not in the period of virus production, and cells infected by both DIPs and natural viruses as well as in the period of virus production. The numbers of the respective cells are denoted by  $C$ ,  $C_V$ ,  $C_V^*$ ,  $C_D$ ,  $C_{VD}$  and  $C_{VD}^*$ , respectively.

Considering infection by DIPs of cells late in the replication cycle is too late to affect the production of the virus, we assume that DIPs cannot infect the cells  $C_V^*$  [24]. There are two age categories for each of the  $C_V$  and the  $C_{VD}$  cells in our model. Ultimately, the DIPs are produced only by the mature  $C_{VD}^*$  cells, and virus particles are produced by both  $C_V^*$  and  $C_{VD}^*$  cells. While  $C_V$  cells can get to maturity by themselves and produce virus,  $C_D$  cells *cannot* produce DIP unless they are co-infected by the virus and become  $C_{VD}$  and get to maturity. The latter models the situation that DIPs cannot replicate unless they co-infect a cell with a wild-type virus.

The following two equations are for modeling the dynamics of the virus and DIP:

$$\begin{aligned} \frac{\partial V}{\partial t} &= \underbrace{d_V \nabla^2 V}_{\text{Diffusion}} + \underbrace{\alpha_1 C_V^* + \alpha_2 C_{VD}^*}_{\text{virus production}} - \underbrace{\delta_V V}_{\text{clearance of virus}}, \\ \frac{\partial D}{\partial t} &= \underbrace{d_D \nabla^2 D}_{\text{Diffusion}} + \underbrace{\alpha_3 C_{VD}^*}_{\text{DIP production}} - \underbrace{\delta_D D}_{\text{clearance of DIP}}, \end{aligned} \quad (1)$$

where  $\nabla^2$  is the Laplacian operator, describing the virus and DIP diffusion.

We assume that cells are not moving in the spatial domain and we can model the dynamics of the cell densities by the following system:

$$\begin{aligned}
 \frac{\partial C_V^*}{\partial t} &= \underbrace{v_1 C_V}_{\text{maturing for virus production}} - \underbrace{\beta_1 C_V^*}_{\text{cell death}}, \\
 \frac{\partial C_{VD}^*}{\partial t} &= \underbrace{v_2 C_{VD}}_{\text{maturing for virus production}} - \underbrace{\beta_2 C_{VD}^*}_{\text{cell death}}, \\
 \frac{\partial C}{\partial t} &= \underbrace{\alpha_C C(1 - C_T/K)}_{\text{Cell growth}} - \underbrace{\gamma_1 C V}_{\text{infected by normal viruses}} - \underbrace{\gamma_2 C D}_{\text{infected by DIPs}} - \underbrace{\delta_C C}_{\text{cell death}}, \\
 \frac{\partial C_V}{\partial t} &= \underbrace{\gamma_1 C V}_{\text{infected by normal viruses}} - \underbrace{\gamma_2 C_V D}_{\text{infected by DIPs}} - \underbrace{v_1 C_V}_{\text{maturing for virus production}} - \underbrace{\delta_{CV} C_V}_{\text{cell death}}, \\
 \frac{\partial C_D}{\partial t} &= \underbrace{\gamma_2 C D}_{\text{infected by DIPs}} - \underbrace{\gamma_1 C_D V}_{\text{infected by normal viruses}} - \underbrace{\delta_{CD} C_D}_{\text{cell death}}, \\
 \frac{\partial C_{VD}}{\partial t} &= \underbrace{\gamma_2 C_V D}_{\text{infected by DIPs}} + \underbrace{\gamma_1 C_D V}_{\text{infected by normal viruses}} - \underbrace{v_2 C_{VD}}_{\text{maturing for virus production}} - \underbrace{\delta_{CVD} C_{VD}}_{\text{cell death}},
 \end{aligned} \tag{2}$$

where  $C_T = C + C_V + C_D + C_{VD} + C_V^* + C_{VD}^*$  is the total density of all cells.

Our model Eqs (1) and (2) is different from that of [24] in several ways: (i) there are two age categories for  $C_{VD}$  cells in our model, but there is no age structure for  $C_{VD}$  cells in [24]; (ii) the mature  $C_{VD}^*$  cells can produce virus in our model, but the  $C_{VD}$  cells in [24] cannot produce virus; (iii)  $C_D$  cells cannot recover to be uninfected cells in our model, but they can recover in [24]; (iv) our parameters  $\gamma_1$  and  $\gamma_2$  can be different, but they are the same in [24].

### Stochastic models in two different scenarios of virus production

Since the outcome of the model with DIPs is sensitive to the competition between viruses and DIPs, different kinds of perturbation to the production of viruses and DIPs may contribute to a huge change in the probability distribution of the outcome. The study in [29] suggested that there are two scenarios of virus production, which can create different kinds of perturbations to virus production:

Scenario 1: infected cells produce virus and DIPs through cell bursting;

Scenario 2: infected cells keep producing viruses and DIPs continuously.

However, these two scenarios cannot be distinguished by our deterministic PDE model [29] as both models with different scenarios have identical mean-field kinetics. In this study, we built a stochastic model and developed an efficient simulation method to examine the effects on the spatial distribution of viruses under different scenarios.

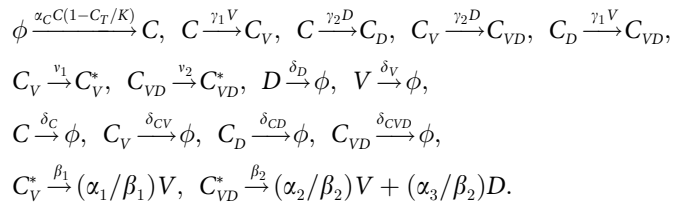
Due to the high computational cost of the spatial stochastic model, there are not many studies considering the effects of different scenarios for virus production on the spreading speed and distribution of the virus. To improve the computational efficiency, here we simulate our model with Spatial Stochastic Simulation Algorithm (SSA) [32], which is a method to generate an exact sample from the probability mass function that is the solution of the chemical master equation.

In SSA, we consider the spatial domain as a two-dimensional square with length  $L$ . The domain is partitioned into  $N_c \times N_c$  identical compartments that are uniform squares with length  $h = L/N_c$ . The subsystem in each compartment is assumed to be homogeneous. The same types of particles and cells in different compartments are treated as different species; for example, we denote by  $V_{i,j}$  the virus level in the compartment at location  $(i, j)$  and consider  $\{V_{1,1}, \dots, V_{1,N_c}, V_{2,1}, \dots, V_{2,N_c}, \dots, V_{N_c,N_c}\}$ . Diffusion is treated as a reaction in which a molecule jumps to one of its neighboring compartments at a constant rate. Then with no-flux boundary conditions (or other conditions which depend on the experimental setting), diffusive jumps obey the following chain reactions for each  $j \in \{1, 2, \dots, N_c\}$ :

$$V_{1,j} \xrightleftharpoons[\rho_1]{\rho_1} V_{2,j} \xrightleftharpoons[\rho_1]{\rho_1} V_{3,j} \cdots \xrightleftharpoons[\gamma]{\rho_1} V_{N_c,j}, \quad V_{j,1} \xrightleftharpoons[\rho_1]{\rho_1} V_{j,2} \xrightleftharpoons[\rho_1]{\rho_1} V_{j,3} \cdots \xrightleftharpoons[\gamma]{\rho_1} V_{j,N_c},$$

where  $\rho_1 = d_V/h^2$ . We assume that  $D_{i,j}$  has similar chain reactions with  $\rho_2 = d_D/h^2$ . We define the *propensity function* for the jumps, for example, at the location  $(i, j)$ , for the four types of jumps (L: left, R: right, U: up, D: down) of virus:  $\alpha_{LV_{ij}}(t) = \rho_1 V_{ij}(t)$ ,  $\alpha_{RV_{ij}}(t) = \rho_1 V_{ij}(t)$ ,  $\alpha_{UV_{ij}}(t) = \rho_1 V_{ij}(t)$ , and  $\alpha_{DV_{ij}}(t) = \rho_1 V_{ij}(t)$ . At the boundary, some jumping directions will not be considered for no-flux boundary conditions. For reactions, we assume that only molecules in the same compartment can react with each other.

Different scenarios of virus production will contain different sets of reactions. In the first scenario, the reactions in the  $(i, j)$  compartment are as follows:



In the second scenario, the reactions (the first three rows of the previous scenario) are the same as the first one except for the production of viruses and DIPs. That is, we replace the last row by the following:



## A new hybrid method for stochastic simulation

In general, the computational cost for a stochastic simulation of a system in two-dimensional domain is extremely high. To reduce the computational cost and maintain the accuracy, we built up a new hybrid method which combines the advantages of our previous works: method of operator splitting [33], and spatially coupled hybrid method with adaptive interface [34]. In the new method, we use operator splitting to improve the efficiency and maintain the accuracy of the simulation; also, through this method with mixing stochastic and deterministic methods, we can apply the hybrid method for specific reactions while keeping others deterministic and hence consider only part of random effects to study which stochastic behavior plays an essential role in the pattern formation.

The hybrid method combines two classes of simulation methods for modeling the reaction processes at two different scales. To capture the advantages of the methods with different scales, we use the method in our previous work [34] to separate the spatial compartments into two types of regions with adaptive interfaces: 1) the regions with “large” numbers of molecules;

2) the regions with “small” numbers of molecules. A more precise criteria for determining “large” and “small” will be given in Eq (3).

To better adapt to the complex system, we separate the compartments for each operator independently. That is, only the number of molecules of the species involved in an operator is considered in the regional division of that operator. We then apply SSA to approximate the dynamics in the region (1), and apply the PDE approximation in the region (2). For coupling two regions, we will apply the pseudo-compartment method [35] with the adaptive interface method we used in [34] in which the locations of the interfaces between different approaches are changing according to the distribution of molecules. With the idea of operator splitting mentioned above [33], our method can provide a numerical framework for studying the spatial stochastic effect of virus transmission. Through this new tool, we will have an efficient method to gain a better understanding about the spatial effect of DIPs in virus transmission.

### The domain and multiple interfaces for different reactions

Consider a general reaction-diffusion system of  $S$  species and  $M$  chemical reactions and diffusion in 4 directions in a two-dimensional domain  $\Omega$ , which is partitioned into  $N_c$  regular compartments of width  $h$ . Let  $N_s(k, t)$  represent the amount of the  $s$ -th species in the  $k$ -th compartment at time  $t$ . Each compartment is small enough so individuals in it can be assumed well mixed.

The subdomain in which we employ the compartment-based regime for the  $j$ -th reaction at time  $t$  is denoted by  $\Omega_c^j(t) \subset \Omega$ , and the other part of  $\Omega$  that employs PDE is represented by  $\Omega_p^j(t)$ .  $\Omega_c^j(t)$  contains all compartments in which the amount of at least one of the reactants in the  $j$ -th reaction is below the threshold value  $\Theta$ . To be specific, assume that reactants of the  $j$ -th reaction are  $\{S_1, S_2, \dots, S_m\}$ . If

$$\min_{i=1,2,\dots,m} \{N_i(k, t)\} < \Theta, \quad (3)$$

then the  $k$ -th compartment is assigned to the stochastic domain  $\Omega_c^j(t)$ , otherwise to the PDE domain  $\Omega_p^j(t)$ . The parameter  $\Theta$  is introduced due to the inherent cut-off in experiments, such as the technical minimum detectable level of RFP/GFP. We tested different values of  $\Theta$  and selected the most appropriate one. In our algorithm, interfaces are adaptive. Domain division and multiple interfaces  $I = \overline{\Omega_p^j(t)} \cap \overline{\Omega_c^j(t)}$  are updated every  $\Delta t_l$ . Fig 2 shows a one-dimensional illustration of the approach stated above.

It's worth noting that  $I^{j_1}$  and  $I^{j_2}$  can be the same if there is an inclusion relationship between the sets of reactants in the  $j_1$ -th and  $j_2$ -th reaction. In fact, the number of non-coincident interfaces is no more than the total number of species in the system. Therefore, compared with a single interface, multiple interfaces can capture stochastic fluctuations more accurately without increasing too much computation costs.

### The pseudo-compartment method

In this section, we will outline the pseudo-compartment method [35], which is the basis of our algorithm. In [35], Yates et al. introduced the pseudo-compartment method for diffusion. On this basis, we propose the possibility of multiple adaptive interfaces.

Consider a reaction-diffusion system of  $S$  species,  $M$  chemical reactions and diffusion in the four directions of the cross in a 2D domain  $\Omega$ . In our algorithm, the PDE region varies for each reaction. So instead of just dividing the PDE based domain, we discretize the whole domain,  $\Omega$ , into a regular grid with spacing  $\Delta x$ . We consider the density of each species. For the  $j$ -th reaction at time  $t$ , the PDE numerical solution is updated for all grid points lie in

## Domain division and interface of $j$ -th reaction

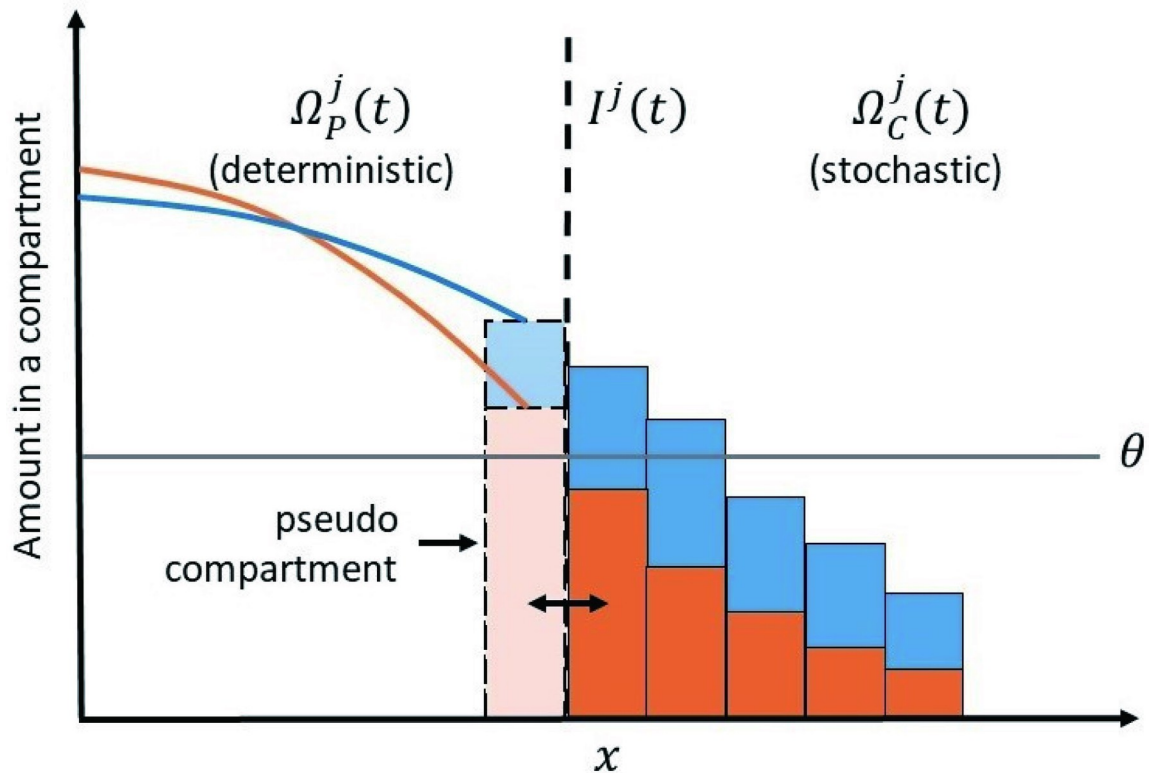


**Fig 2. An illustration of the domain division and interface of the  $j$ -th reaction.** Here we show an example with two reactants. The domain  $\Omega_p^j(t)$  is modeled by PDE and the domain  $\Omega_c^j(t)$  is modeled by compartment-based SSA. The amount of each species in a compartment in  $\Omega_p^j(t)$  is  $\int_{C_k} p_s(x, t) dx$ . If any reactant amount is below the threshold  $\Theta$ , then that compartment is part of  $\Omega_c^j(t)$ . Individuals can move between the boundary compartment of  $\Omega_c^j(t)$  and the pseudo-compartment in  $\Omega_p^j(t)$ . In the two-dimensional case, diffusion takes four directions: up, down, left and right.

<https://doi.org/10.1371/journal.pcbi.1011513.g002>

$\Omega_p^j(t)$ . Diffusion terms are treated in a similar way, but employing the implicit Euler method. A zero-flux boundary condition is implemented in  $\Omega_p^j(t)$ , including domain boundaries and interfaces. Flux at the interface is implemented in the compartment-based regime.

The compartment-based regime evolves from the Gillespie algorithm (SSA). Consider the propensity function of reactions and diffusion,  $\alpha_{i,j}(t)$ , for compartment  $C_i \subset \Omega_c^j(t)$ .  $\alpha_{i,j}(t)dt$  represents the probability that the  $j$ -th reaction (for  $j \in \{1, \dots, M+4\}$ , including diffusion) occurs in  $C_i$  during the small time interval  $[t, t+dt]$ .

The coupling is implemented with a pseudo-compartment,  $C_{-1}$ , presented for diffusion between the deterministic and stochastic domains. This is a compartment adjacent to the interface but within deterministic domain  $\Omega_p^j(t)$ , where  $j \in \{M+1, \dots, M+4\}$ , representing diffusion (four directions of the cross). In order to correctly model the flux over the interface, individuals in the boundary compartment in  $\Omega_c^j$  can jump into the pseudo-compartment with the usual diffusive rate, and vice versa. The amount of each species within the pseudo-compartment is calculated through direct integration of the PDE,

$$N_s(-i, t) = \int_{C_{-1,i}} p_s(x, t) dx, \quad (4)$$

where  $p_s(x, t)$  is the PDE solution of density of the  $s$ -th species. Then the propensity function for jumping from the pseudo-compartment to the adjoining compartment in  $\Omega_C^j(t)$  is given by

$$\alpha_{ij}^*(t) = \frac{N_s(-i, t)D_s}{h^2} = \frac{D_s}{h^2} \int_{C_{-1,i}} p_s(x, t) dx, \quad j = M + 1, \dots, M + 4. \quad (5)$$

The Gillespie's direct method [36] is used to simulate the time evolution of stochastic regime. The time interval for next reaction,  $\tau$ , is determined by:

$$\left\{ \begin{array}{l} \alpha_0 = \sum_{j=1}^{M+4} \sum_{C_j \in \Omega_C^j(t)} \alpha_{ij}^*(t) + \sum_{j=M+1}^{M+4} \sum_{C_{-1,i} \in \Omega_P^j(t)} \alpha_{ij}^*(t), \\ \tau = \frac{1}{\alpha_0} \ln \frac{1}{r_1}, \end{array} \right. \quad (6)$$

where  $r_1$  is a random variable uniformly distributed in  $(0, 1)$ . We then use the second random number  $r_2$  to find the corresponding reaction or jump. The algorithm then checks whether the closer update time is for PDE or SSA. If  $t + \tau < t_P$ , then the update is for SSA and  $t = t + \tau$ ; otherwise it is for PDE and  $t = t_P$ ,  $t_P = t + \Delta t_P$ .

## Moving interface

The multiple interfaces are updated with time step  $\Delta t_I$ , by recomparing amounts in a compartment of all reactants of each reaction with the threshold  $\Theta$ . Similar to [37], after the interfaces are updated, we need to keep numbers in the stochastic domain as integer values, but we cannot simply get rid of the fractional parts. Suppose the compartment  $C_k$  is moved from the PDE domain to the stochastic domain, and the fractional part is

$$P = \left\{ \int_{C_k} p(x, t) dx \right\}, \quad (7)$$

where  $\{\cdot\}$  is the fractional part function.  $P$  is used as the probability that an additional individual is kept in this compartment. We then take a uniform random number  $r \in [0, 1]$ . If  $r < P$  then we place the individual in compartment  $C_k$ ; otherwise it is placed in the deterministic domain.

The pseudocode for our algorithm is given in Algorithm 1.

### Algorithm 1 The hybrid algorithm for reaction-diffusion systems.

1. Initialize the time,  $t = t_0$  and set the final time,  $T$ . Specify the PDE-update time step  $\Delta t_P$  and initialize the next PDE time step to be  $t_P = t + \Delta t_P$ . Specify the interface-update time step  $\Delta t_I$  and initialize the next interface-update time step to be  $t_I = t + \Delta t_I$ .
2. Specify the PDE spacial step  $\Delta x$  and the compartment width  $h$ . Initialize the amount of each species in each compartment,  $N_s(k, t)$  for  $k \in \{1, \dots, K\}$  and specify the threshold  $\Theta$ . Compute the density,  $p_s(x, t) = N_s(k, t)/h$  for PDE grid points.
3. Determine the initial interface for each reaction  $j$ ,  $j \in \{1, 2, \dots, M\}$ :
  - (a) Find all  $k$  such that  $\min_{s \in S_j} \{N_s(k, t)\} < \Theta$ , where  $S_j$  contains all species involved in reaction  $j$ , then the  $k$ -th compartment is part of the stochastic domain  $\Omega_C^j$ , and otherwise part of the PDE domain  $\Omega_P^j$ .
  - (b) All compartments adjacent to  $\Omega_C^j$  (no diagonal angles) are regarded as pseudo compartments.
4. Determine the time for the next 'compartment-based' event according to the Gillespie algorithm,  $t_C = t + \tau$ .

5. If  $\min\{t_C, t_P, t_I\} = t_C$  then the next compartment-based event occurs:
  - (a) Determine which event occurs according to the Gillespie algorithm.
  - (b) If the event is moving from stochastic domain to a pseudo compartment,  $C_{-1}$ , then for the corresponding  $(s, k)$ ,  $N_s(k, t + \tau) = N_s(k, t) - 1$  and  $p(x, t + \tau) = p(x, t) + \mathbb{I}_{[x \in C_{-1}]} / h$ . Here,  $\mathbb{I}_{[x \in A]}$  is an indicator function that takes the value 1 when  $x \in A$  and 0 otherwise.
  - (c) If the event is moving from a pseudo compartment  $C_{-1}$  to stochastic domain and  $p(x, t) > 1/h$  for all  $x \in C_{-1}$ , then  $N_s(k, t + \tau) = N_s(k, t) + 1$  and  $p(x, t + \tau) = p(x, t) - \mathbb{I}_{[x \in C_{-1}]} / h$ .
  - (d) Update the density for the pseudo compartment.
  - (e) Update the current time,  $t = t_C$ .
6. If  $\min\{t_C, t_P, t_I\} = t_P$  then the PDE domain is updated:
  - (a) Apply backward Euler for diffusion terms and forward Euler for reaction terms.
  - (b) Update the density for the pseudo compartment.
  - (c) Update the current time,  $t = t_P$  and set  $t_P = t + \Delta t_P$ .
7. If  $\min\{t_C, t_P, t_I\} = t_I$  then the interfaces are updated, similar to step 3:
  - (a) For each reaction, find all  $k$  such that  $\min_{s \in S_j} \{N_s(k, t)\} < \Theta$ , where  $S_j$  contains all species involved in reaction  $j$ , then the  $k$ -th compartment is part of the stochastic domain  $\Omega_C^j$ , and otherwise part of the PDE domain  $\Omega_P^j$ .
  - (b) All compartments adjacent to  $\Omega_C^j$  (no diagonal angles) are regarded as pseudo compartments.
  - (c) For the compartment  $C_k$  that change from PDE domain to stochastic domain, let  $P_s = \{\int_{C_k} p_s(x, t) dx\}$ . Take a random number  $r_s \in [0, 1]$ .
    - If  $r_s < P_s$  then  $N_s(k, t_I) = \text{ceil}(N_s(k, t))$  and  $p_s(x, t_I) = p_s(x, t) - (1 - P_s) / \text{Area}(\Omega_P^j)$  for  $x \in \Omega_P^j$ ;
    - otherwise,  $N_s(k, t_I) = \text{floor}(N_s(k, t))$  and  $p_s(x, t_I) = p_s(x, t) + P_s / \text{Area}(\Omega_P^j)$  for  $x \in \Omega_P^j$ .
  - (d) Update the current time,  $t = t_I$  and set  $t_I = t + \Delta t_I$ .
8. If  $t \leq T$ , return to step 4.  
Else end.

## Parameter selection

We consider the spatial domain as a two-dimensional square with length  $L = 2.552\text{mm}$ , which is the same as the experimental data; for the PDE numerical scheme, we apply the central difference scheme to discretize the Laplace operation with  $\Delta x = \Delta y = 0.058\text{mm}$ ; for the temporal numerical scheme, we use the backward Euler method for the Laplace operation and forward Euler method for the other terms with time step  $\Delta t = 0.01\text{h}$ . In the SSA approximation, the domain is partitioned into square compartments with dimension  $h \times h = \Delta x \times \Delta y$ .

Diffusion coefficients of virus and DIP are set to be  $2.38 \times 10^{-6}\text{cm}^2$  in [31] while the decay rate is  $4.0 \times 10^{-5}\text{s}^{-1}$ . As the diffusion rate varies according to the environment and plays a vital role in spatial distribution, we increased the former  $d_V = d_D = 2.38 \times 10^{-3}\text{mm}^2/\text{h}$  to provide qualitative agreement with experimental data and left the latter unchanged  $\delta_V = \delta_D = 0.144\text{h}^{-1}$ .

In [27], the rate of virus production is expressed as the product of the number of viruses released per cell after packaging and the rate at which each cell produces viruses. Therefore  $\alpha_1 = 758.045 \times (68.503 \times 10^{\pm 2}\text{d}^{-1}) = 2163.682 \times 10^{\pm 2}\text{h}^{-1}$ , and  $\alpha_3 = 38.259 \times (21.782 \times 10^{\pm 2}\text{d}^{-1}) = 34.723 \times 10^{\pm 2}\text{h}^{-1}$ . The wide range of parameters allows us to choose a suitable value to obtain a good agreement with the experimental results qualitatively. So we set  $\alpha_1 = 6.491\text{h}^{-1}$  and

Table 1. Parameters used in the simulations.

Parameter	Definition	Value	Reference
$d_V$	Diffusion coefficient of virus	$2.38 \times 10^{-3} \text{ mm}^2/\text{h}$	[31]
$d_D$	Diffusion coefficient of DIP	$2.38 \times 10^{-3} \text{ mm}^2/\text{h}$	[31]
$\alpha_1$	Rate of virus production from virus-infected cell	$6.491 \text{ h}^{-1}$	[27]
$\alpha_2$	Rate of virus production from co-infected cell	$\alpha_3/10$	this work
$\alpha_3$	Rate of DIP production from co-infected cell	$69.446 \text{ h}^{-1}$	[27]
$\alpha_C$	Rate of uninfected cell proliferation	$0.634 \text{ h}^{-1}$	[27]
$K$	Cellular carrying capacity of proliferation	$3.505 \times 10^5 \times h^2 \text{ cell/compartment}$	[27]
$\nu_1$	Rate of maturation of $C_V$ cells into $C_V^*$ cells	$0.205 \text{ h}^{-1}$	[27]
$\nu_2$	Rate of maturation of $C_{VD}$ cells into $C_{VD}^*$ cells	$0.205 \text{ h}^{-1}$	[27]
$\beta_1$	Death rate of $C_V^*$	0.05	[27]
$\beta_2$	Death rate of $C_{VD}^*$	0.05	[27]
$\gamma_1$	Virus infection rate	$4 \times 10^{-4} \text{ h}^{-1}$	this work
$\gamma_2$	DIP infection rate	$4 \times 10^{-4} \text{ h}^{-1}$	this work
$\delta_V$	Virus decay rate	$0.144 \text{ h}^{-1}$	[31]
$\delta_D$	DIP decay rate	$0.144 \text{ h}^{-1}$	[31]
$\delta_C$	Death rate of cells	$0.059 \text{ h}^{-1}$	[31]
$\delta_{CV}$	Death rate of cells	$0.059 \text{ h}^{-1}$	[31]
$\delta_{CD}$	Death rate of cells	$0.059 \text{ h}^{-1}$	[31]
$\delta_{CVD}$	Death rate of cells	$0.059 \text{ h}^{-1}$	[31]

<https://doi.org/10.1371/journal.pcbi.1011513.t001>

$\alpha_3 = 69.446 \text{ h}^{-1}$ . Since DIPs may exhibit a replication advantage over infectious viruses [3], we assumed  $\alpha_2 = \alpha_3/10$  in this work.

Same as [27], the intrinsic rate of uninfected cell proliferation is  $\alpha_C = 15.217 \text{ d}^{-1} = 0.634 \text{ h}^{-1}$ . But the cellular carrying capacity of proliferation varies depending on the experimental environment. We let  $K = 3.505 \times 10^5 \times h^2$  cells/compartment to achieve qualitative agreement with experimental data, where  $h^2$  is the compartment area.

The rate of maturation of  $C_V$  cells into  $C_V^*$  cells is  $9.863 \times 10^{\pm 2} \text{ d}^{-1}$  in [27]. We slightly increase it to  $\nu_1 = \nu_2 = 0.205 \text{ h}^{-1}$  because mature infected cells are observed later in experiments.  $\beta_1$  and  $\beta_2$  are considered as the death rate of  $C_V^*$  and that of  $C_V$  respectively, which are  $2.426 \times 10^{\pm 2} \text{ d}^{-1}$  in [27]. We take  $\beta_1 = \beta_2 = 0.05 \text{ h}^{-1}$  in simulations.

Virus and DIP infection rate is  $2.45 \times 10^{-10} = 1.02 \times 10 \text{ d}^{-1} = 1.02 \times 10^{-11} \text{ h}^{-1}$  in [27], which is relatively small. Different experiments and higher cell density may lead to a larger infection rate. Hence we set  $\gamma_1 = \gamma_2 = 4 \times 10^{-4} \text{ h}^{-1}$ .

The infected cell death rate is  $5.91 \times 10^{-2} \text{ h}^{-1}$  in [31], which is used as death rates for all cells in our simulations.

All parameters are listed in Table 1. It is worth noting that our set of parameters can guarantee that species in the system without DIPs will coexist in the following simulations. A detailed proof is provided in S1 Appendix.

## Interpretation of experimental data

To validate the usefulness of our model, we compare the simulation results with the experiment data published in [3], the latter is composed of time series of images obtained via Microscopy from the co-propagation of infectious and defective viruses in a population of biological cells. These co-infection experiments were initiated with the same virus inputs (MOI 30) but different DIP inputs (namely MOI 0, 1, 10 and 84). and microscopy images were taken at 7

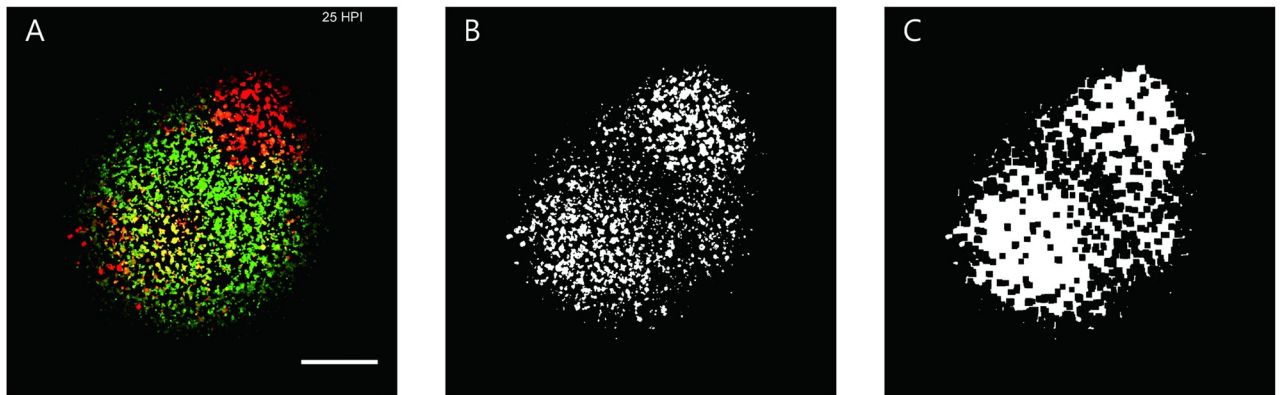


**Fig 3. A representative example of interpreting the preprocessing of experimental figures.** A: An original experiment figure. B: The red single channel is extracted (virus expression) and denoised. C: Morphological transformations (dilation followed by erosion).

<https://doi.org/10.1371/journal.pcbi.1011513.g003>

hours, 13 hours, 19 hours and 25 hours post infection. The DIP expresses a green fluorescent protein (GFP) and the wild-type virus expresses a red fluorescent protein (RFP). There are three to five time series for each of the RFP intensity and the GFP intensity. Each image has size of (2200, 2200) with diameter of 1.16  $\mu\text{m}$  pixel. The scale bar is 0.5 mm.

Fluorescent protein labeling is usually used for qualitative purposes, and there is no linear relationship between brightness and intensity. Therefore the experimental images only provide a reference for virus expression in simulations.

Since in the following simulations we employed the compartment-based method while experiments provide scatter diagrams, we have done some preprocessing to compare them with the computer simulation results. Fig 3A is a representative experiment figure. We extracted the red single channel (the virus is expressed) and filtered noise, as shown in Fig 3B. We then did morphological transformations (dilation followed by erosion) to close small holes inside the objects. Therefore Fig 3C maintains the critical features of virus expression in experiments and is more approximate to compartment-based.

## Results

### Dynamics and pattern formation of virus expression

We first study the PDE model in Eqs (1) and (2). Fig 4 shows the spatial distribution of  $C_V^*$  and  $C_{VD}^*$  in a 2D domain at time  $t = 25\text{h}$  with different initial DIPs, as well as images of experimental data at the same time in [3]. When there is no DIP, viruses are uniformly radially distributed in both simulations and experiments. When the initial condition is  $C_{VD}(0) = 200$  for the PDE model, then viruses are distributed in a ring while the DIPs are radially distributed in the center. Compared with the experimental results under similar conditions, the PDE model shows good agreement in the speed of infection with experimental data but the spatial distribution does not match and the patchiness of  $C_V^*$  is not observed in PDE simulations.

In stochastic simulations, the same types of particles and cells in different compartments are treated as different species, for example, for  $V$ , denoted by

$\{V_{1,1}, \dots, V_{1,N_c}, V_{2,1}, \dots, V_{2,N_c}, \dots, V_{N_c,N_c}\}$ . The initial condition is  $V_{i,j}(0) = D_{i,j}(0) = C_{Vi,j}^*(0) = C_{VDi,j}^*(0) = C_{Di,j}(0) = 0$  and  $C_{i,j}(0) = 1000$  for all  $(i, j)$ ,  $C_{Vi,j}(0) = C_{VDi,j}(0) = 0$  for all  $(i, j)$  except the midpoint  $C_{V22,22}(0) = 100$ , and  $C_{VD22,22}(0)$  varies from 0 to 400.

Two scenarios are considered in simulations and compared with experimental results:

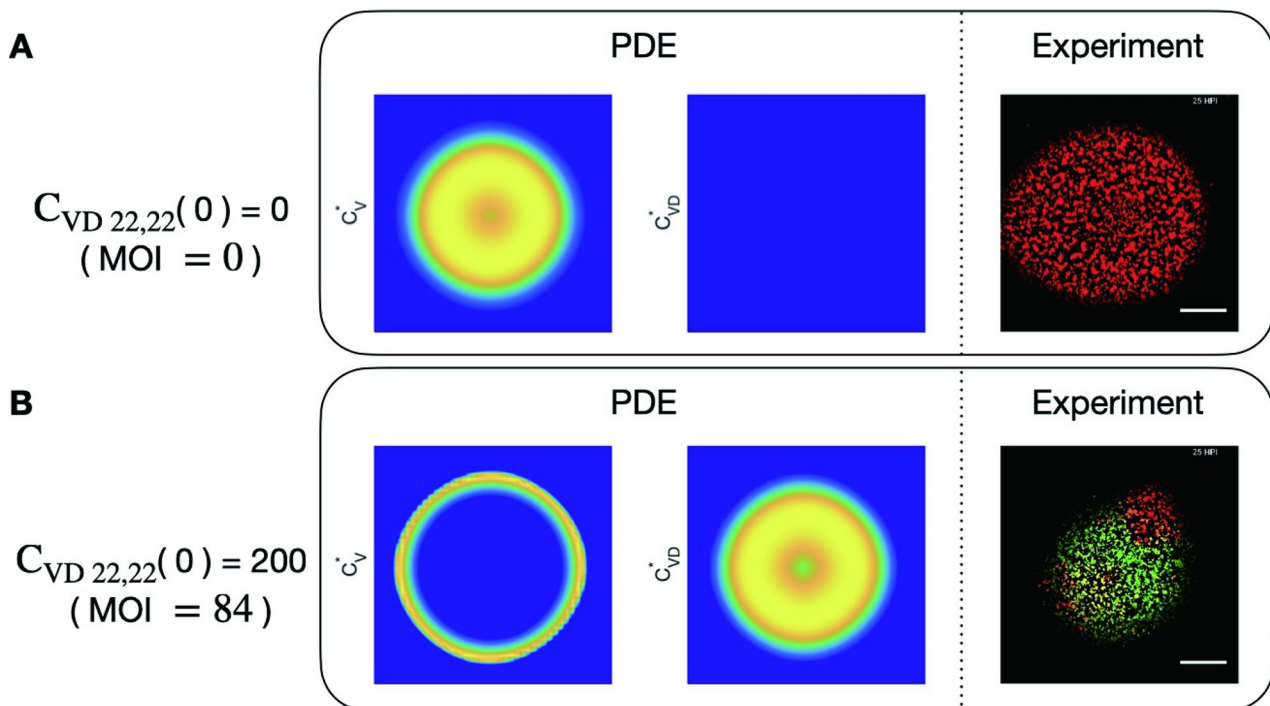


**Fig 4. Spatial distributions of virus and DIP in cells in PDE simulations and experiments.** A: Spatial distributions of virus in cells ( $C_V$ ) and DIP in cells ( $C_{VD}$ ) in PDE simulations and representative experiment with initial DIP equal to 0. B: Spatial distributions of virus in cells ( $C_V$ ) and DIP in cells ( $C_{VD}$ ) in PDE simulations and representative experiment with initial DIP equal to 84.

<https://doi.org/10.1371/journal.pcbi.1011513.g004>

Scenario 1: infected cells produce virus and DIPs through cell bursting;

Scenario 2: infected cells keep producing viruses and DIPs continuously.

Fig 5 shows the evolution of viruses in cells and DIPs in cells without initial DIP from  $t = 17\text{h}$  to  $t = 25\text{h}$ . Row 1 and 2 show the spatial distribution of matured infected cells  $C_V^*$  and  $C_{VD}^*$ , which is proportional to viral expression and DIP—virus expression in Scenario 1 and Scenario 2, at time  $t = 17\text{ h}$  and  $t = 25\text{ h}$  respectively. The experimental observation has an inherent threshold, and images have been denoised; therefore, we also introduced a cut-off for simulation data. Namely the amount of cells is set to be zero if it is less than the cut-off value 50, which is also applied to all the following simulations. The last column is the evolution of a representative experiment without initial DIP. When there is no DIP in the system initially, there is no DIP growth, and the virus growth is radially symmetric and flat in both scenarios and experiments.

In experiments, the radial symmetry disappears as the initial amount of DIP increases. In fact, patchy formation of cells infected by virus is sensitive to the dose of DIP. It can be observed even with a small initial dose of DIP (Fig 6). When the initial DIP is raised from 10 to 84 in experiments, the majority of the virus at the end is concentrated (see Fig 7 and S1 Fig). Simulations show similar results, but Scenario 1 shows a much higher probability of forming a pattern than S2 and matches the experimental data better. In scenario S1, infected cells produce viruses and DIPs through cell bursting, and then viruses and DIPs diffuse, which leads to a more accidental position; while in Scenario 2, infected cells keep producing viruses and DIPs, meaning the location of those cells will continuously produce virus and DIPs. Hence the spatial distribution is more centralized rather than patchy.

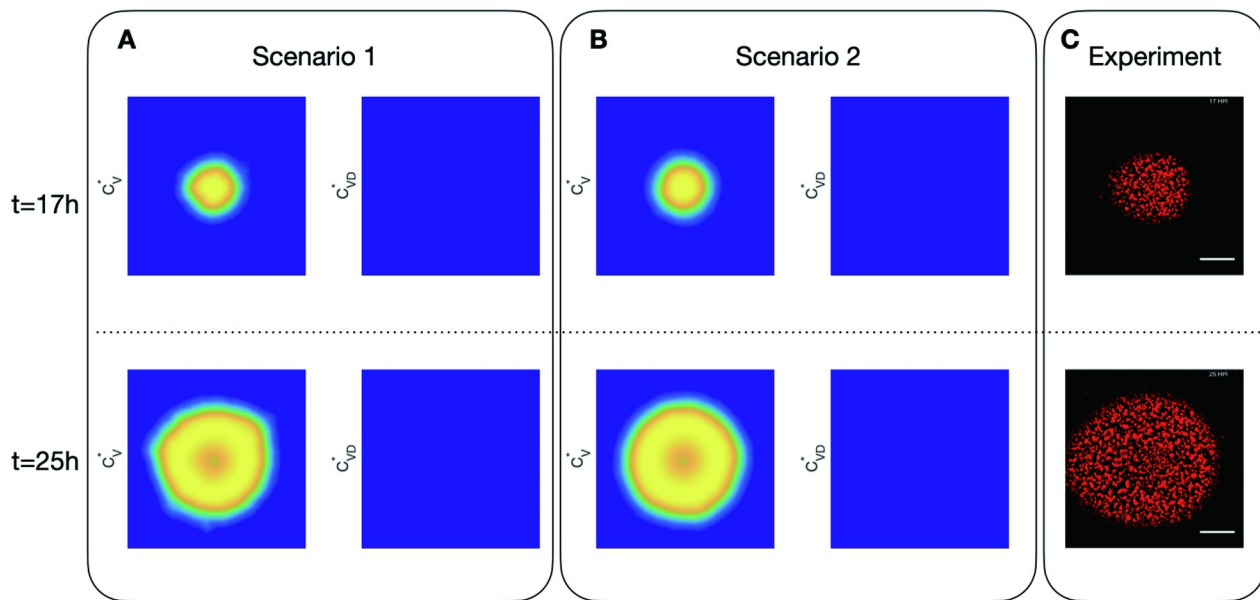


**Fig 5. Dynamics of virus and DIP in cells in 2 scenarios simulations and representative experiment with initial DIP equal to 0.** A: spatial distribution of virus in cells ( $C_v^*$ ) and DIP in cells ( $C_{VD}^*$ ) in Scenario 1 (infected cells produce virus and DIPs through cell bursting) at time  $t = 17\text{h}$  and  $t = 25\text{h}$ ; B: spatial distribution of those in Scenario 2 (infected cells keep producing viruses and DIPs); C: the representative experimental results.

<https://doi.org/10.1371/journal.pcbi.1011513.g005>

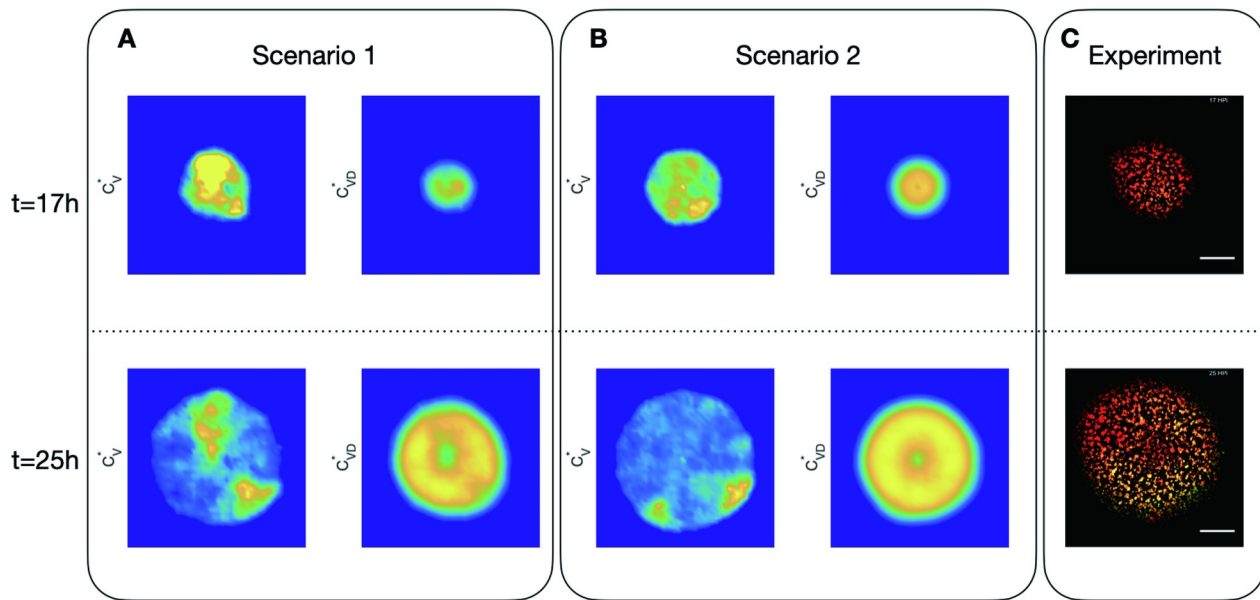


**Fig 6. Dynamics of virus and DIP in cells in 2 scenarios simulations with  $C_{VD22,22}(0) = 4$  and representative experiment with initial DIP equal to 1.** A: spatial distribution of virus in cells ( $C_v^*$ ) and DIP in cells ( $C_{VD}^*$ ) in Scenario 1 (infected cells produce virus and DIPs through cell bursting) at time  $t = 17\text{h}$  and  $t = 25\text{h}$ ; B: spatial distribution of those in Scenario 2 (infected cells keep producing viruses and DIPs); C: the representative experimental results.

<https://doi.org/10.1371/journal.pcbi.1011513.g006>

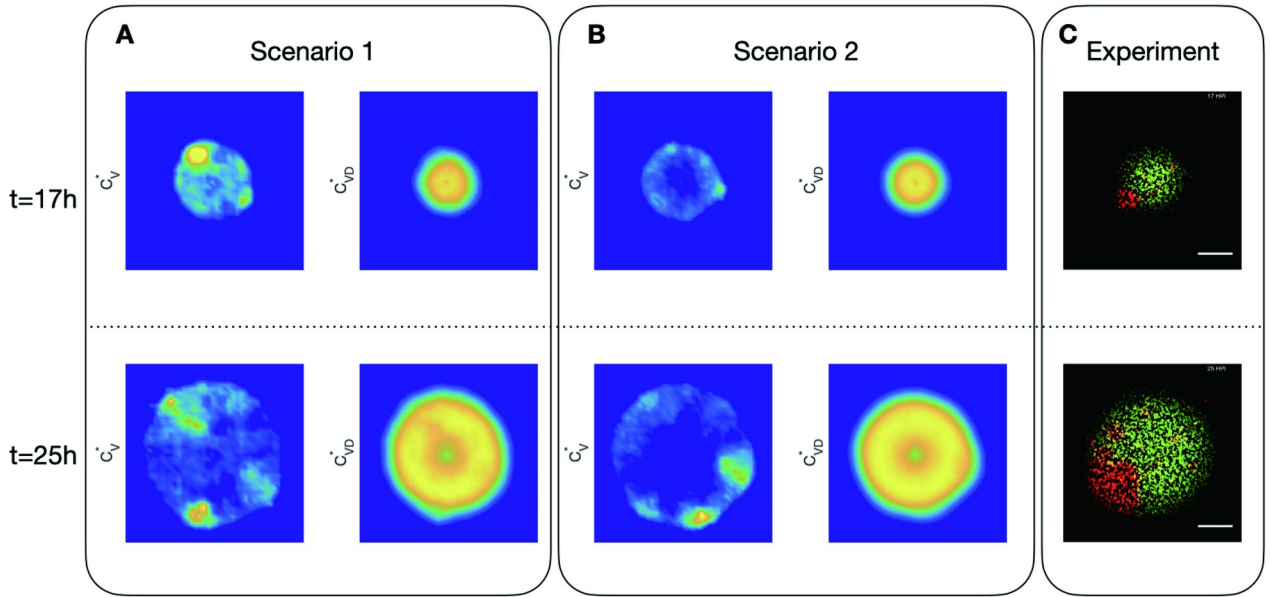


**Fig 7. Dynamics of virus and DIP in cells in 2 scenarios simulations with  $C_{VD22,22}(0) = 40$  and representative experiment with initial DIP equal to 10.** A: spatial distribution of virus in cells ( $C_V$ ) and DIP in cells ( $C_{VD}$ ) in Scenario 1 (infected cells produce virus and DIPs through cell bursting) at time  $t = 17\text{h}$  and  $t = 25\text{h}$ ; B: spatial distribution of those in Scenario 2 (infected cells keep producing viruses and DIPs); C: the representative experimental results.

<https://doi.org/10.1371/journal.pcbi.1011513.g007>

### Spread rate of virus

To quantify the spread characteristics of viral expression under stochastic effects, we define the virus radius as:

$$R(t) = \sqrt{\frac{\text{Area}(C_V(x, y, t))}{\pi}}, \quad (8)$$

where  $C_V(x, y, t)$  represents the amount of cells infected by virus at grid point  $(x, y)$  at time  $t$ . Since a certain amount of virus expression is required to be observed in the experiment and noise is filtered, we also set a cut-off  $\theta = 50$  for computing area, i.e.

$$\text{Area}(C_V(x, y, t)) = \sum_{(x, y)} \mathbb{I}_{C_V(x, y, t) > \theta} \Delta x \Delta y. \quad (9)$$

For experimental data, a detailed illustration is in Fig 3. Fig 8 shows the radius of virus versus time  $9 \leq t \leq 25$  (h) with different initial DIP inputs in 2 scenarios simulations and experiments. We can see the radius keeps increasing and viruses keep spreading in all cases. Whereas as initial DIPs increase, in both experiments and simulations, the growth rate of radius goes down, which is due to the inhibitory effect of DIPs on viruses. On the other hand, the Scenario 1 can better match the experimental results, both in terms of the dynamics and the level of fluctuations.

We note that after a certain time, the plague radius grows linearly with respect to time for each fixed initial dose of DIPs, and studied the relationship between the virus radius growth rate and initial DIP dose. To get rid of the difference in units of initial conditions in simulations and experiments, we consider a dimensionless ratio  $\rho = \frac{C_{VD}(0)}{C_V(0)}$ . Since initial viruses remain the same,  $\rho$  is proportional to initial DIPs. Fig 9 shows the relationship between the

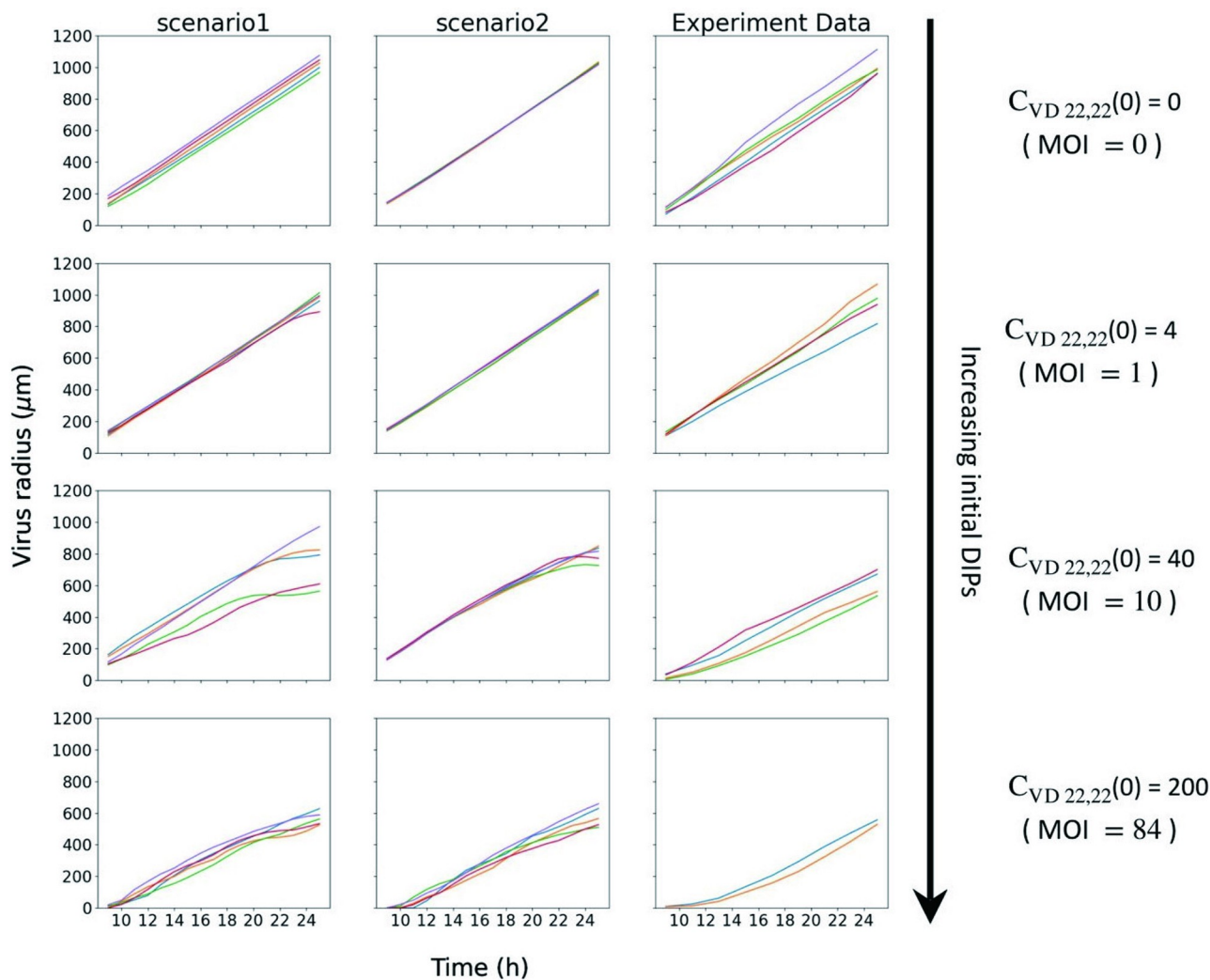


**Fig 8. Radius of virus against time with different initial DIP inputs in 2 scenarios simulations and experiments.** In each subfigure, curves in different colors are different simulations (or experiments) with the same initial conditions. The initial conditions for the same row are the same.

<https://doi.org/10.1371/journal.pcbi.1011513.g008>

virus radius growth rate and initial DIP dose intuitively. We used a logarithmic  $x$ -axis, so it is shifted by 0.01 to avoid troubles when  $\rho = 0$ . The growth rate was computed using the data points after  $t = 13$  h to ensure in all cases we have close to linear growth in radius vs. time (slope of lines in Fig 8). We run 50 group simulations for each initial condition to compute the average. When there is no DIP in the system, the virus radius growth rates are the same in both scenarios; as initial DIPs increase, the growth rate drops dramatically, which means DIPs slow down the growth of virus particles.

### Patchiness via $q$ -statistic

Patchy spatial patterns are typically observed in the image data when the initial dose of DIP is large enough. To quantify the patchiness of the image data, we employ a standard spatial statistic called the  $q$ -statistic [38]. We choose this statistic because it is suitable for our data and convenient to implement. The definition of this statistic depends on our choice of strata, which is

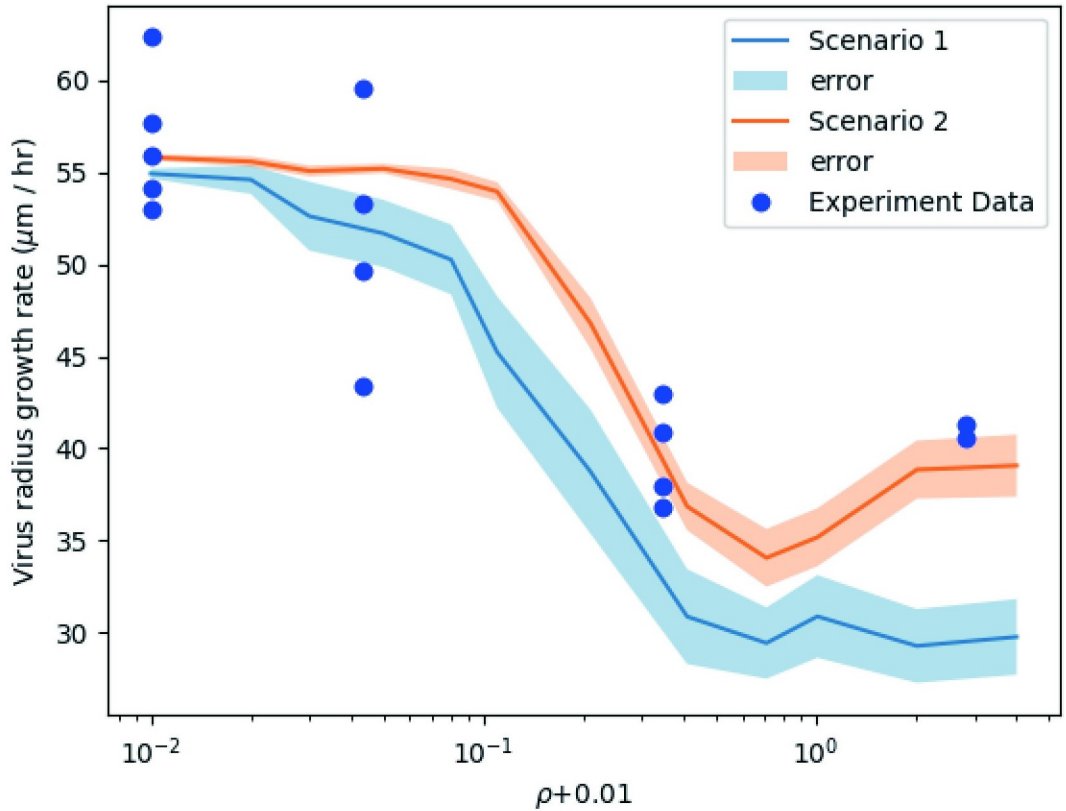


**Fig 9. The growth rate of virus radius against initial DIP inputs in 2 scenarios simulations and experiments.** The x-axis is a logarithmic scale and the errors are described by the 95% confidence intervals.

<https://doi.org/10.1371/journal.pcbi.1011513.g009>

a decomposition of the image data. In our case, the entire image is divided into 30 sectors with an equal ratio of the angle to form 30 strata  $S = \{L_1, L_2, \dots, L_{30}\}$  and the union of  $L_i$  is the whole plaque  $P$ . A visual illustration is as shown in S2 Fig. In our case, since experiments employed qualitative rather than quantitative methods, that is, we can see viral expression at all fluorescent points but the brightness of these points is not proportional to the intensity. So we convert all figures binary and  $M(i, j, t)$  denotes the brightness at the  $(i, j)$ -th pixel at time  $t$  for the image, which range is  $\{0, 255\}$ . For simulation results, we set a threshold for the binary transformation to approximate the threshold inherent in the experimental methods and offset the loss when denoising the experimental images. Specifically, when  $C_V^* < 50$ ,  $M = 0$  and the point is black in the image; when  $C_V^* \geq 50$ ,  $M = 255$  and the point is red (an example in S3 Fig). Then, the  $q$ -statistics is defined to be

$$q_t = 1 - \frac{\sum_{L \in S} \sum_{(i,j) \in L} \left( M(i, j, t) - \bar{M}_L^t \right)^2}{\sum_{(i,j) \in P} \left( M(i, j, t) - \bar{M}_P^t \right)^2} \\ = 1 - \frac{1}{N\sigma^2} \sum_{L \in S} N_L \sigma_L^2, \quad (10)$$

where  $\bar{M}_A^t = \frac{\sum_{(i,j) \in A} M(i, j, t)}{|A|}$  and  $|A|$  is the cardinality of set  $A$ .  $N$ ,  $N_h$ ,  $\sigma$ ,  $\sigma_h$  denote the number of pixels in the entire image, the number of pixels in each stratum, the standard deviation of the

entire image and the standard deviation of each stratum, respectively. This statistic is invariant under spatial scale and remains the same if the intensity of the image is multiplied by a factor.

A more intuitive formula for the  $q$ -statistic is as follows [38], here we omit the time dependence, meaning denote  $M(i, j, t)$  by  $M_{i,j}$  and  $q_t$  by  $q$ ; The denominator of Eq (10) can be written as

$$\sum_{L \in S} \sum_{(i,j) \in L} (M_{i,j} - \overline{M}_L)^2 + \sum_{L \in S} |L| (\overline{M}_L - \overline{M}_P). \quad (11)$$

Call those two terms the sum of squares within strata (SSW) and the sum of squares between strata (SSB) and note that the numerator of Eq (10) is exactly SSW, so

$$q = 1 - \frac{SSW}{SSW + SSB}. \quad (12)$$

So if  $q \approx 1$ , that means the sum of squares within strata is relatively more minor, indicating in each stratum, the virus is concentrated and the sum of squares between strata is somewhat more significant, meaning the differences between strata are large, so the image would appear to be more patchy. If  $q \approx 0$ , the variance in each stratum is large, and the differences between strata are minor, so the picture would appear to be not so patchy. The  $q$ -statistic provides a suitable and convenient way to quantify the patchiness that are visibly observed in the experimental data we studied in this work. By choosing different strata according to the data, like rectangular grid in a non-radially symmetric system and triangular mesh for surfaces, this method may be applicable to other studies of spatial temporal systems.

We study the behavior of  $q$ -statistic of cells infected by the virus at time  $t = 25$  h, that is  $C_V^*(25)$  in simulations, when the initial dose of DIPs varies. To get rid of the difference in units, we consider a dimensionless ratio  $\rho = \frac{C_{VD}(0)}{C_V(0)}$ . Since we always keep the initial viruses constant,  $\rho$  is proportional to the initial dose of DIPs.

In Fig 10, the  $x$ -axis is a logarithmic scale so we shift it by 0.01 to the right to avoid trouble when  $\rho = 0$  (initial DIP is zero). On the left, the blue line denotes the  $q$ -statistic of Scenario 1 (infected cells produce viruses and DIPs through cell bursting) while the red line denotes that of Scenario 2 (infected cells keep producing viruses and DIPs) at time  $t = 25$  h. The errors are

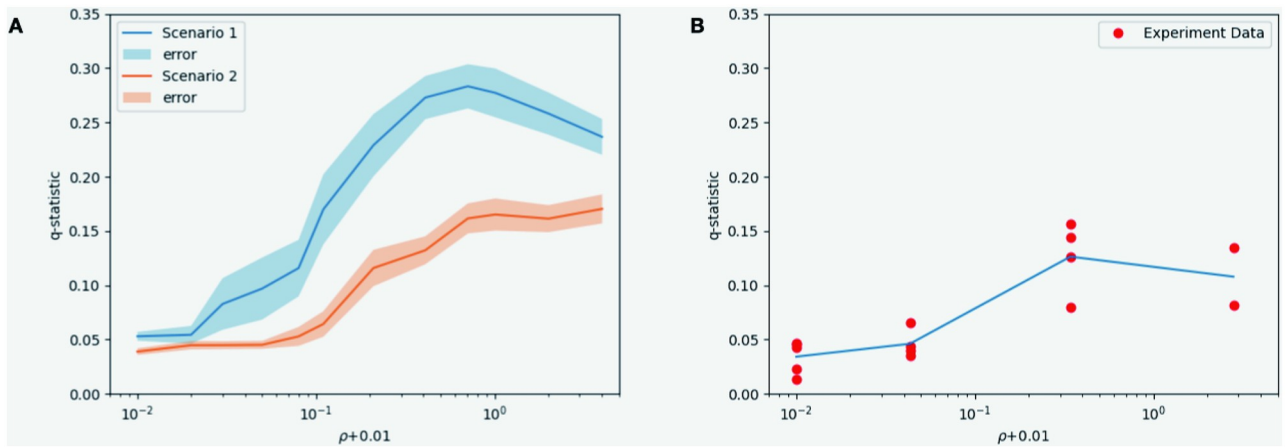


**Fig 10. The average  $q$ -statistics of  $C_V^*$  against initial DIP inputs at time  $t = 25$  h in 2 scenarios simulations and experiments.** A: the blue (red) line is the  $q$ -statistic of Scenario 1 (Scenario 2), and the bands show the 95% confidence intervals; B: the  $q$ -statistic for each experimental image.

<https://doi.org/10.1371/journal.pcbi.1011513.g010>

described by the 95% confidence intervals. On the right, we marked the  $q$ -statistic for each experimental image at time  $t = 25$  h and plot the average for four groups of experiments. Both scenarios show the same trend as experiments. When there is no DIP in the beginning, the  $q$ -statistic is minor, meaning the spatial distribution is uniform. The  $q$ -statistic increases as the initial dose of DIPs increases. Taking into account the conclusions of the previous section, DIPs slow down the growth of virus particles and make them more patchy. But when the initial dose of DIP is large enough, we observe a drop of  $q$ -statistic. It may be caused by the domination of DIPs. To be specific, when the infection of DIPs is dominated, cells infected by the virus are distributed as sporadic patches and the majority of the domain is homogeneous ( $C_v^* = 0$ ). The  $q$ -statistic is sensitive to the changes in DIPs. On the other hand, Scenario 2 shows a closer magnitude of  $q$ -statistic to experimental data while that of Scenario 1 is relatively higher. In fact, Scenario 1 leads to a higher level of amount of  $C_v^*$  and larger size of patterns. When infected cells produce viruses and DIPs through cell bursting, their positions are more stochastic, and hence there is a larger probability of patchy formation, which also explains the wider confidence interval of Scenario 1.

## Discussion

DIPs can co-infect a cell with viable viruses and interfere with virus production [1, 3]. However, the mechanism by which DIPs affect the spatial distribution of virus expression is still unclear.

In this work, we constructed a PDE model to describe the interaction between viruses and DIPs in a two-dimensional domain. Moreover, to study the stochastic effect on spatial dynamics of the virus spreading and patchy formation, we developed a stochastic reaction-diffusion system to describe the system in two different scenarios of virus production. In Scenario 1, infected cells produce viruses and DIPs through cell bursting. Therefore the position of virus production is accidental, which leads to a higher probability of patchy formation. In Scenario 2, infected cells keep producing viruses and DIPs. The virus is produced continuously at the cell position, making the spatial distribution concentrated in one point. As shown in Fig 10, compared to Scenario 2, Scenario 1 has a higher  $q$ -statistic value under the same conditions. The reason is that Scenario 1 results in a higher level of  $C_v^*$  and a larger size of patterns. In Scenario 2, more area has no  $C_v^*$  and hence is flat. In addition, Scenario 1 shows the non-monotonicity; that is, when the initial dose of DIP is large enough, we observe a drop of  $q$ -statistic in Scenario 1. A potential reason is that cells infected by the virus lose domination due to stochastic extinction and are distributed as sporadic patches. Further work is needed to quantify the conditions and mechanisms for this initial drop. The patchy pattern observed in the experiments can be regenerated in our stochastic simulation results. Our model provides a good framework for studying reaction-diffusion systems under stochastic effects.

We also built a hybrid algorithm for stochastic simulation. Classical stochastic methodologies are computationally intensive in two-dimensional cases. Our algorithm is based on the pseudo-compartment method [35] and introduces adaptive multiple interfaces to adjust complex systems. It combines two scales of simulation methods for modeling the reaction processes and can capture the advantages of the methods with different scales. It improves computational efficiency and maintains critical stochastic features. Our method can provide a numerical framework for studying the spatial stochastic effect of other biological systems and is compatible with different scale stochastic study methods like stochastic differential equations.

We measured the spread rate of the virus and showed the relationship between the spread radius growth rate and the initial dose of DIP. To measure the patchiness, we computed the  $q$ -

statistic. Our simulations can simultaneously capture two spatial spread features (patchiness and spread rate) in wet-lab experimental data, which was not achieved in previous works. In previous studies, there were not many models considering the spatial effects of DIP-virus interaction. Deterministic models in one or two dimensions were developed but could not simultaneously capture the spread rate and the spatial patterns observed in experiments [24, 25]. A stochastic model has been established in [29] to investigate different solutions for continuous and burst production of viruses that cannot be studied by deterministic models.

Another stochastic model supports a slowing effect of DIPs on the growth of viral plaques, but the spread features are not quantified [31]. Here we consider two mechanisms for virus production and simultaneously regenerate the patchy patterns and spread rates observed in experiments. It supports that the DIPs slow down the growth of virus particles and make them more patchy. These methods and statistics are useful tools to understand and explain the diverse spatial-temporal features in complex biological systems. For example, it is known that advection can also play an important role in the passive mass transfer of infectious particles in tissue culture [39, 40]. The pattern of infection spread in [3] arises from autocatalytic reaction (virus reproduction) and diffusion (of free virus particles), without any contribution from advection or convection (fluid flow). In [3] the authors used a semi-solid agar overlay on top of the cells that prevents any fluid flow, so the only motion is diffusion of free virus particles, forming plaques. By contrast, in [41] (see Fig 1), the authors used a liquid overlay, where subtle changes in fluid density owing to evaporative cooling allowed outward radial fluid flows (convection) to sweep across the cells as virus was released, giving rise to ‘comet-like’ infections that span much greater distances. We expect the computing methods and statistics we developed in this paper are useful in studying advection and different spatial movements in complex biological systems and to compare experimental and simulation results.

## Supporting information

**S1 Appendix. Virus infection without DIPs.**  
(PDF)

**S1 Fig. Dynamics of virus and DIP in cells in 2 scenarios simulations with  $C_{VD22,22}(0) = 200$  and representative experiment with initial DIP equal to 84.** A: spatial distribution of virus in cells ( $C_V^*$ ) and DIP in cells ( $C_{VD}^*$ ) in Scenario 1 (infected cells produce virus and DIPs through cell bursting) at time  $t = 17$ h and  $t = 17$ h; B: spatial distribution of those in Scenario 2 (infected cells keep producing viruses and DIPs); C: the representative experimental results.  
(EPS)

**S2 Fig. Strata used in the computation of  $q$ -statistics.**  
(EPS)

**S3 Fig. A representative example to illustrate the image processing of simulation results for computing the  $q$ -statistic.** A: the spatial distribution of  $C_V^*$  in 2D with the same color bar as Figs 5–7, which is then converted to binary. B: all points where  $C_V^* < 50$  are black ((0,0,0) in RGB); otherwise, they are red ((255,0,0) in RGB).  
(EPS)

**S4 Fig. Dynamics of virus and DIP in cells in PDE simulations and experiments.** A: Time series plot of virus in cells ( $C_V^*$ ) and DIP in cells ( $C_{VD}^*$ ) growth in PDE simulations and representative experiment with initial DIP equal to 0. B: Time series plot of virus in cells ( $C_V^*$ ) and DIP in cells ( $C_{VD}^*$ ) growth in PDE simulations and representative experiment with initial DIP

equal to 84.  
(EPS)

**S5 Fig. Dynamics of virus and DIP in cells in 2 scenarios simulations with  $C_{VD22,22}(0) = 0$  and representative experiment with initial DIP equal to 0.** Row 1, 2 are time series plots of virus in cells ( $C_V^*$ ) and DIP in cells ( $C_{VD}^*$ ) growth in Scenario 1 (infected cells produce virus and DIPs through cell bursting); Row 3, 4 are time series plots of those in Scenario 2 (infected cells keep producing viruses and DIPs); Row 5 is the representative experimental results.  
(EPS)

**S6 Fig. Dynamics of virus and DIP in cells in 2 scenarios simulations with  $C_{VD22,22}(0) = 4$  and representative experiment with initial DIP equal to 1.** Row 1, 2 are time series plots of virus in cells ( $C_V^*$ ) and DIP in cells ( $C_{VD}^*$ ) growth in Scenario 1 (infected cells produce virus and DIPs through cell bursting); Row 3, 4 are time series plots of those in Scenario 2 (infected cells keep producing viruses and DIPs); Row 5 is the representative experimental results.  
(EPS)

**S7 Fig. Dynamics of virus and DIP in cells in 2 scenarios simulations with  $C_{VD22,22}(0) = 40$  and representative experiment with initial DIP equal to 10.** Row 1, 2 are time series plots of virus in cells ( $C_V^*$ ) and DIP in cells ( $C_{VD}^*$ ) growth in Scenario 1 (infected cells produce virus and DIPs through cell bursting); Row 3, 4 are time series plots of those in Scenario 2 (infected cells keep producing viruses and DIPs); Row 5 is the representative experimental results.  
(EPS)

**S8 Fig. Dynamics of virus and DIP in cells in 2 scenarios simulations with  $C_{VD22,22}(0) = 200$  and representative experiment with initial DIP equal to 84.** Row 1, 2 are time series plots of virus in cells ( $C_V^*$ ) and DIP in cells ( $C_{VD}^*$ ) growth in Scenario 1 (infected cells produce virus and DIPs through cell bursting); Row 3, 4 are time series plots of those in Scenario 2 (infected cells keep producing viruses and DIPs); Row 5 is the representative experimental results.  
(EPS)

## Acknowledgments

The authors are grateful to Dr. John Yin for helpful discussions and for sharing the data in [3].

## Author Contributions

**Conceptualization:** Qiantong Liang, Johnny Yang, Wai-Tong Louis Fan, Wing-Cheong Lo.

**Formal analysis:** Qiantong Liang, Johnny Yang.

**Investigation:** Qiantong Liang.

**Methodology:** Qiantong Liang, Johnny Yang, Wai-Tong Louis Fan, Wing-Cheong Lo.

**Supervision:** Wai-Tong Louis Fan, Wing-Cheong Lo.

**Writing – original draft:** Qiantong Liang.

**Writing – review & editing:** Qiantong Liang, Johnny Yang, Wai-Tong Louis Fan, Wing-Cheong Lo.

## References

1. Frensing T. Defective interfering viruses and their impact on vaccines and viral vectors. *Biotechnology journal*. 2015; 10(5):681–9. <https://doi.org/10.1002/biot.201400429> PMID: 25728309
2. Pesko KN, Fitzpatrick KA, Ryan EM, Shi P-Y, Zhang B, Lennon NJ, et al. Internally deleted WNV genomes isolated from exotic birds in New Mexico: function in cells, mosquitoes, and mice. *Virology*. 2012; 427(1):10–7. <https://doi.org/10.1016/j.virol.2012.01.028> PMID: 22365325
3. Baltes A, Akpinar F, Inankur B, Yin J. Inhibition of infection spread by co-transmitted defective interfering particles. *PloS one*. 2017; 12(9):e0184029. <https://doi.org/10.1371/journal.pone.0184029> PMID: 28915264
4. Walters RW, Freimuth P, Moninger TO, Ganske I, Zabner J, Welsh MJ. Adenovirus fiber disrupts CAR-mediated intercellular adhesion allowing virus escape. *Cell*. 2002; 110(6):789–99. [https://doi.org/10.1016/S0092-8674\(02\)00912-1](https://doi.org/10.1016/S0092-8674(02)00912-1) PMID: 12297051
5. Bhuvanakantham R, Chong M-K, Ng M-L. Specific interaction of capsid protein and importin- $\alpha/\beta$  influences West Nile virus production. *Biochemical and biophysical research communications*. 2009; 389(1):63–9. <https://doi.org/10.1016/j.bbrc.2009.08.108> PMID: 19712667
6. Ge Q, Filip L, Bai A, Nguyen T, Eisen HN, Chen J. Inhibition of influenza virus production in virus-infected mice by RNA interference. *Proceedings of the National Academy of Sciences*. 2004; 101(23):8676–81. <https://doi.org/10.1073/pnas.0402486101> PMID: 15173599
7. Shirogane Y, Rousseau E, Voznica J, Xiao Y, Su W, Catching A, et al. Experimental and mathematical insights on the interactions between poliovirus and a defective interfering genome. *PLoS pathogens*. 2021; 17(9):e1009277. <https://doi.org/10.1371/journal.ppat.1009277> PMID: 34570820
8. Akpinar F, Timm A, Yin J. High-throughput single-cell kinetics of virus infections in the presence of defective interfering particles. *Journal of virology*. 2016; 90(3):1599–612. <https://doi.org/10.1128/JVI.02190-15> PMID: 26608322
9. Rezelj VV, Carrau L, Merwaiss F, Levi LI, Erazo D, Tran QD, et al. Defective viral genomes as therapeutic interfering particles against flavivirus infection in mammalian and mosquito hosts. *Nature Communications*. 2021; 12(1):2290. <https://doi.org/10.1038/s41467-021-22341-7> PMID: 33863888
10. Dropulić B, Hěrmánková M, Pitha PM. A conditionally replicating HIV-1 vector interferes with wild-type HIV-1 replication and spread. *Proceedings of the National Academy of Sciences*. 1996; 93(20):11103–8. <https://doi.org/10.1073/pnas.93.20.11103> PMID: 8855316
11. Noble S, McLain L, Dimmock NJ. Interfering vaccine: a novel antiviral that converts a potentially virulent infection into one that is subclinical and immunizing. *Vaccine*. 2004; 22(23–24):3018–25. <https://doi.org/10.1016/j.vaccine.2004.02.013> PMID: 15297051
12. Li D, Lin M-H, Rawle DJ, Jin H, Wu Z, Wang L, et al. Dengue virus-free defective interfering particles have potent and broad anti-dengue virus activity. *Communications biology*. 2021; 4(1):557. <https://doi.org/10.1038/s42003-021-02064-7> PMID: 33976375
13. Wodarz D, Hofacre A, Lau JW, Sun Z, Fan H, Komarova NL. Complex spatial dynamics of oncolytic viruses in vitro: mathematical and experimental approaches. *PLoS computational biology*. 2012; 8(6):e1002547. <https://doi.org/10.1371/journal.pcbi.1002547> PMID: 22719239
14. Saenz RA, Quinlivan M, Elton D, MacRae S, Blunden AS, Mumford JA, et al. Dynamics of influenza virus infection and pathology. *Journal of virology*. 2010; 84(8):3974–83. <https://doi.org/10.1128/JVI.02078-09> PMID: 20130053
15. Getto P, Kimmel M, Marciniak-Czochra A. Modelling and analysis of dynamics of viral infection of cells and of interferon resistance. *Journal of mathematical analysis and applications*. 2008; 344(2):821–50. <https://doi.org/10.1016/j.jmaa.2008.02.069>
16. Perelson AS. Modelling viral and immune system dynamics. *Nature reviews immunology*. 2002; 2(1):28–36. <https://doi.org/10.1038/nri700> PMID: 11905835
17. Heldt FS, Kupke SY, Dorl S, Reichl U, Frensing T. Single-cell analysis and stochastic modelling unveil large cell-to-cell variability in influenza A virus infection. *Nature communications*. 2015; 6(1):8938. <https://doi.org/10.1038/ncomms9938> PMID: 26586423
18. Perelson AS, Ribeiro RM. Modeling the within-host dynamics of HIV infection. *BMC biology*. 2013; 11:1–10. <https://doi.org/10.1186/1741-7007-11-96> PMID: 24020860
19. Pawelek KA, Huynh GT, Quinlivan M, Cullinane A, Rong L, Perelson AS. Modeling within-host dynamics of influenza virus infection including immune responses. *PLoS computational biology*. 2012; 8(6):e1002588. <https://doi.org/10.1371/journal.pcbi.1002588> PMID: 22761567
20. Graw F, Perelson AS. Modeling viral spread. *Annual review of virology*. 2016; 3:555–72. <https://doi.org/10.1146/annurev-virology-110615-042249> PMID: 27618637

21. Whitman J, Dhanji A, Hayot F, Sealfon SC, Jayaprakash C. Spatio-temporal dynamics of host-virus competition: a model study of influenza A. *Journal of Theoretical Biology*. 2020; 484:110026. <https://doi.org/10.1016/j.jtbi.2019.110026> PMID: 31574283
22. Yin J, Redovich J. Kinetic modeling of virus growth in cells. *Microbiology and Molecular Biology Reviews*. 2018; 82(2). <https://doi.org/10.1128/MMBR.00066-17> PMID: 29592895
23. Kirkwood T, Bangham C. Cycles, chaos, and evolution in virus cultures: a model of defective interfering particles. *Proceedings of the National Academy of Sciences*. 1994; 91(18):8685–9. <https://doi.org/10.1073/pnas.91.18.8685>
24. Frank SA. Within-host spatial dynamics of viruses and defective interfering particles. *Journal of theoretical biology*. 2000; 206(2):279–90. <https://doi.org/10.1006/jtbi.2000.2120> PMID: 10966764
25. Akpinar F, Inankur B, Yin J. Spatial-temporal patterns of viral amplification and interference initiated by a single infected cell. *Journal of Virology*. 2016; 90(16):7552–66. <https://doi.org/10.1128/JVI.00807-16> PMID: 27279621
26. Laske T, Heldt FS, Hoffmann H, Frensing T, Reichl U. Modeling the intracellular replication of influenza A virus in the presence of defective interfering RNAs. *Virus Research*. 2016; 213:90–9. <https://doi.org/10.1016/j.virusres.2015.11.016> PMID: 26592173
27. Mapder T, Clifford S, Aaskov J, Burrage K. A population of bang-bang switches of defective interfering particles makes within-host dynamics of dengue virus controllable. *PLoS computational biology*. 2019; 15(11):e1006668. <https://doi.org/10.1371/journal.pcbi.1006668> PMID: 31710599
28. Saxena A, Byram PK, Singh SK, Chakraborty J, Murhammer D, Giri L. A structured review of baculovirus infection process: Integration of mathematical models and biomolecular information on cell–virus interaction. *Journal of General Virology*. 2018; 99(9):1151–71. <https://doi.org/10.1099/jgv.0.001108> PMID: 30027883
29. Pearson JE, Krapivsky P, Perelson AS. Stochastic theory of early viral infection: continuous versus burst production of virions. *PLoS computational biology*. 2011; 7(2):e1001058. <https://doi.org/10.1371/journal.pcbi.1001058> PMID: 21304934
30. Immonen T, Gibson R, Leitner T, Miller MA, Arts EJ, Somersalo E, et al. A hybrid stochastic–deterministic computational model accurately describes spatial dynamics and virus diffusion in HIV-1 growth competition assay. *Journal of theoretical biology*. 2012; 312:120–32. <https://doi.org/10.1016/j.jtbi.2012.07.005> PMID: 22814476
31. Clark NR, Tapia KA, Dandapani A, MacArthur BD, Lopez C, Maayan A. Stochastic model of virus and defective interfering particle spread across mammalian cells with immune response. *arXiv preprint arXiv:11084901*. 2011.
32. Smith CA, Yates CA. Spatially extended hybrid methods: a review. *Journal of the Royal Society Interface*. 2018; 15(139):20170931. <https://doi.org/10.1098/rsif.2017.0931> PMID: 29491179
33. Lo W-C, Zheng L, Nie Q. A hybrid continuous-discrete method for stochastic reaction–diffusion processes. *Royal Society open science*. 2016; 3(9):160485. <https://doi.org/10.1098/rsos.160485> PMID: 27703710
34. Lo W-C, Mao S. A hybrid stochastic method with adaptive time step control for reaction–diffusion systems. *Journal of Computational Physics*. 2019; 379:392–402. <https://doi.org/10.1016/j.jcp.2018.11.042>
35. Yates CA, Flegg MB. The pseudo-compartment method for coupling partial differential equation and compartment-based models of diffusion. *Journal of The Royal Society Interface*. 2015; 12(106):20150141. <https://doi.org/10.1098/rsif.2015.0141> PMID: 25904527
36. Gillespie DT. Exact stochastic simulation of coupled chemical reactions. *The journal of physical chemistry*. 1977; 81(25):2340–61. <https://doi.org/10.1021/j100540a008>
37. Spill F, Guerrero P, Alarcon T, Maini PK, Byrne H. Hybrid approaches for multiple-species stochastic reaction–diffusion models. *Journal of computational physics*. 2015; 299:429–45. <https://doi.org/10.1016/j.jcp.2015.07.002> PMID: 26478601
38. Wang J-F, Zhang T-L, Fu B-J. A measure of spatial stratified heterogeneity. *Ecological indicators*. 2016; 67:250–6. <https://doi.org/10.1016/j.ecolind.2016.02.052>
39. Yakimovich A, Yakimovich Y, Schmid M, Mercer J, Sbalzarini IF, Greber UF. Infectio: a generic framework for computational simulation of virus transmission between cells. *MspHERE*. 2016; 1(1). <https://doi.org/10.1128/mSphere.00078-15> PMID: 27303704
40. Doceul V, Hollinshead M, van der Linden L, Smith GL. Repulsion of superinfecting virions: a mechanism for rapid virus spread. *Science*. 2010; 327(5967):873–6. <https://doi.org/10.1126/science.1183173> PMID: 20093437
41. Zhu Y, Yin J. A quantitative comet assay: Imaging and analysis of virus plaques formed with a liquid overlay. *Journal of virological methods*. 2007; 139(1):100–2. <https://doi.org/10.1016/j.jviromet.2006.09.006> PMID: 17092573